

Cite this: *Soft Matter*, 2012, **8**, 7004

www.rsc.org/softmatter

PAPER

Stochastic rate-dependent elasticity and failure of soft fibrous networks

A. S. Abhilash,^a Prashant K. Purohit^b and Shailendra P. Joshi^{*a}

Received 26th February 2012, Accepted 3rd May 2012

DOI: 10.1039/c2sm25450f

This work focuses on modeling the rate-sensitive stiffening-to-softening transition in fibrous architectures mimicking crosslinked fibrous actin (F-actin) networks induced by crosslink unbinding. Using finite element based discrete network (DN) modeling combined with stochastic crosslink scission kinetics, we correlate the microstructural damage evolution with the macroscopic stress–strain responses of these networks as a function of applied deformation rate. Simulations of multiple DN realizations for fixed filament density indicate that an incubation strain exists, which characterizes the minimum macroscopic deformation that a network should accrue before damage initiates. This incubation strain exhibits a direct relationship with the applied strain rate. Simulations predict that the critical damage fraction corresponding to colossal softening is quite low, which may be ascribed to the network non-affinity and filament reorientation. Furthermore, this critical fraction appears to be independent of applied strain rate. Based on these characteristics, we propose a phenomenological damage evolution law mimicking scission kinetics in an average sense. This law is embedded within an existing continuum model that is extended to include non-affine effects induced by filament bending.

1 Introduction

Fibrous networks are often found to be structural motifs over a wide range of length-scales in both natural and artificial structural systems. Of particular interest are those that exist at the microscopic length-scales. Examples of such microscopic fibrous networks include biopolymers, elastomers, hydrogels, paper, carbon nanotube architectures and many more.^{1–5} These micro-architectures render mechanical robustness to the structural systems they constitute. F-actin filament networks in biological cells are an important class of such fibrous architectures that play key role in various cellular functions like mechanotransduction, mitosis and cell-migration.^{6–12} From a mechanics perspective, such fibrous networks are exciting micro-architectures that provide avenues to devise efficient functional solutions for a variety of engineering applications.^{13,14}

The mechanical behavior of biopolymeric networks ensues from the rich dynamics that arise from the properties and topological arrangements of their constituents. They exhibit an initial soft response followed by a rate-dependent nonlinear stiffening that may culminate in a precipitous drop in the overall stiffness beyond a critical strain.^{15–19} The nonlinear stiffening has been attributed to entropic elasticity and/or a bending-stretching transition of the semiflexible filaments that is modulated by crosslink [actin binding proteins (ABP)]

behavior.^{3,17,18,20–29} While much of the modeling focus has been on networks with rigid crosslinks, recent efforts have been on understanding the role of crosslink deformability^{15,16} and molecular motors³⁰ on the overall transient network response. Experiments indicate that networks may soften reversibly through filament buckling,^{31,32} or irreversibly as crosslinks dissociate under local tensile forces.^{19,33} There seem to be compelling reasons to develop a mechanism-based failure description of such soft, fibrous architectures as they may signal plasticity or failure of the network architecture, which in turn relate to important functional consequences.^{15,19} However, the irreversible softening mechanics are not accounted for in most works or are largely phenomenological.^{28,34}

In this paper, we investigate the mechanics of fibrous architectures mimicking semi-flexible F-actin networks. We develop a finite element (FE) based DN approach incorporating topological randomness and stochastic crosslink scission kinetics. We demonstrate that the kinetics of the crosslink scission process give rise to a rate-dependent stiffening and failure of these discrete, fibrous networks. The DN approach is rendered particularly useful, because the failure mechanics is governed by local details of a microstructure rather than just the average characteristics. The stochastic approach to modeling the crosslink dissociation process coupled with the topological variations of networks (for the same nominal parameters, *e.g.* filament density) introduce statistical effects in their mechanical behavior. The rate-dependent stiffness evolution and the peak stiffness obtained through DN calculations corroborate reasonably with experimental observations. Importantly, the DN simulations provide the rate-dependent evolution of crosslink scission as

^aDepartment of Mechanical Engineering, National University of Singapore, 117576, Singapore. E-mail: shailendra@nus.edu.sg; Tel: +65-6516 4496

^bMechanical Engineering and Applied Mechanics, University of Pennsylvania, Philadelphia, PA 19104, USA

a function of the applied strain. This information is valuable in constructing continuum damage models for such microstructures. We demonstrate one such example of a homogenized continuum model with an evolutionary internal variable representing the crosslink scission process.

2 Discrete network model of F-actin networks

Real *in vitro* F-actin networks are random architectures of undulated F-actin filaments connected by crosslinking proteins and surrounded by a fluid medium.³⁵ Apart from the filament length L , another important length-scale in such networks is l_p , the filament persistence length which is in the range of ~ 10 to $20 \mu\text{m}$.³⁶ When $l_p \gg L$, undulated filaments act as if they were straight. Van der Giessen and co-workers showed that the macroscopic responses of networks assuming straight filaments is qualitatively similar to those modeled using undulated filaments;^{27,37} initial undulations tend to postpone the transition from flimsy to stiff behavior. Therefore, we model the networks with straight filaments with individual filaments designed to be of length $L \approx l_p$. For a prescribed line (filament) density $\bar{\rho}$, our in-house MATLAB® code generates a 2D network of randomly oriented straight filaments that intersect each other at discrete points within the computational window (Fig. 1). These intersection points are considered as crosslinks and are modeled as springs with finite stiffness. We perform a topological analysis to check the randomness of the initial average orientation of a generated network (see Appendix A for a brief discussion). The code automatically generates an FE mesh on the topology and records the necessary information in a manner that can be seamlessly read into ABAQUS/CAE®.³⁸

The unfolding characteristics of the crosslinks are approximated by a bi-linear constitutive relationship comprising an initial compliant regime followed by a highly stiff behavior.^{16,34,39,40} The unbinding characteristic of a crosslink is tantamount to the

scission process beyond which it is incapable of supporting any load. Interestingly, the critical force F_{cr} for scission exhibits a rate-effect that depends logarithmically on the applied loading rate.^{41,42} Another equally striking experimental observation is the variability of F_{cr} for a fixed loading rate.^{42,43} This variability, even at the single crosslink level, is expected to play a role in the overall network response. A noteworthy feature incorporated in the present work is that it explicitly accounts for this rate-dependent stochastic crosslink dissociation process. This is achieved by combining the Bell model,⁴⁴ which gives an exponential relation to the applied force and the dissociation rate, with a kinetic Monte Carlo (KMC) algorithm.⁴⁵ The crosslink dissociation rate is given by

$$k_{\text{off}} = k_{\text{off}}^0 e^{(Fa/k_B T)} \quad (1)$$

where k_{off}^0 is the characteristic dissociation rate in the absence of applied force, F is the induced local tensile force on a crosslink, a is the interaction distance,^{46,47} k_B is the Boltzmann constant and T is the temperature. The stochastic crosslink scission is introduced as a KMC step in that the crosslink life-time is given by

$$t = -\frac{1}{k_{\text{off}}} \log(r) \quad (2)$$

where $0 < r < 1$ is a uniformly distributed random number. A crosslink may potentially dissociate if it satisfies the criterion

$$t \leq \hat{t} \quad (3)$$

where $\hat{t} = \varepsilon_c / \dot{\varepsilon}$ with $\dot{\varepsilon}$ being the local axial strain rate and $\varepsilon_c = a/l_0$ being the critical axial dissociation strain for a crosslink of length l_0 .

The time-scales associated with the crosslink dissociation kinetics may interact with the time-scale pertaining to the macroscopic deformation rate, producing an overall rate-dependent network response including stiffening and failure.^{18,46} In the model system adopted here, we consider that $\bar{\rho} = 10$ that translates to an actin concentration of $\sim 0.8 \text{ mg ml}^{-1}$.⁴⁸ From a numerical viewpoint, we model a square computational domain of fixed size, $W = 40 \mu\text{m}$. From this, the total number of filaments N in the computational domain is obtained through the relationship $\bar{\rho} = NL^2/W^2$, where $L = 10 \mu\text{m}$.²¹ Filaments are meshed using 2D Euler–Bernoulli beam finite elements and each crosslink is modeled using a spring element having both axial and transverse degrees of freedom while the rotational degree of freedom is unconstrained. We adopt the parameters that resemble networks crosslinked by filamin, which is a relatively compliant ABP among the myriad crosslinkers that have been reported in the literature.¹⁹ The parameters used in the crosslink scission algorithm are $k_{\text{off}}^0 = 0.1 \text{ s}^{-1}$, $a = 0.5 \text{ nm}$ and $l_0 = 160 \text{ nm}$.^{47,49} Note that at every time-step there may be multiple crosslinks that satisfy eqn (3), but we choose to break only the one with the smallest t . The reader is referred to Appendix B for the implementation of KMC algorithm in FE framework.⁴⁵

We note here that similar to the scission process, crosslink reformation is also an important phenomenon that ascertains that the network remains structurally viable, e.g. thermally activated crosslink scission. However, the scission rate is enhanced exponentially in the presence of tension F in a crosslink. More generally, the equilibrium constant of the reaction is



Fig. 1 Initial configuration of a typical network. Dangling ends are removed and the boundary of the computational window (red dashed lines) along with the kinematic boundary conditions (b.c.'s) are shown.

given by $\hat{k}(F) = (k_{\text{off}}/k_{\text{on}}) = \hat{k}_0 e^{(F/k_s T)}$, where k_{on} is the rate of crosslink formation, \hat{k} is the equilibrium constant and \hat{k}_0 is the value of \hat{k} at zero force.⁴⁶ If the tensile force in a filament is large then the reaction is biased toward crosslink scission and may prevail over the relinking process, although the former may provide sites for the latter. The crosslink rebinding phenomenon is rich with complexities⁵⁰ and is beyond the scope of this paper.

3 Discrete network simulation results

For the given $\bar{\rho}$, Fig. 1 shows the initial configuration of one of the many realizations considered in this work. The kinematic boundary conditions (b.c.'s) prescribed on the edges of the computational domain are as follows: the bottom edge is fixed while the top edge is sheared horizontally with a constant velocity \bar{v} , simulating simple shear condition with a nominal shear strain rate $\dot{\gamma} = \bar{v}/W$. Periodic b.c.'s are applied to the left and right edges so that the microstructure can be considered as representative of an infinitely long slab in the horizontal direction.

In order to investigate the rate effects, we shear a given network at $\dot{\gamma} = 0.01, 0.1$ and 1.0 s^{-1} . Fig. 2 shows snapshots of the final configurations of the network for these shear rates. The flexibility of the crosslinks is evident from the extensive deformation at the filament intersections (blue springs). The crosslink dissociation is more severe at low rates due to the low critical breaking force. It is interesting to note the tendency of the network to form *stress fibers*, which may be construed as a set of aligned filaments that are closely bundled together, traversing the principal tensile axis. These stress fibers are more commonly observed at higher rates (e.g. Fig. 2c) compared to lower rates.

In what follows, we first discuss the deterministic mechanics of one network topology (Fig. 2) in order to provide an insight into the macro-micro nexus. A deterministic analysis implies that the stochastic step (eqn (2)) is not activated in the simulations. Then, we discuss the rate-dependent behavior of the networks in terms of the stiffness and the evolution of crosslink scission. Following that, we discuss the stochastic effects arising from the KMC procedure and the variability arising from topological randomness (for fixed $\bar{\rho}$). Finally, we present a homogenized continuum model with damage. The damage evolution in a network with applied strain is characterized by the crosslink scission fraction ϕ .

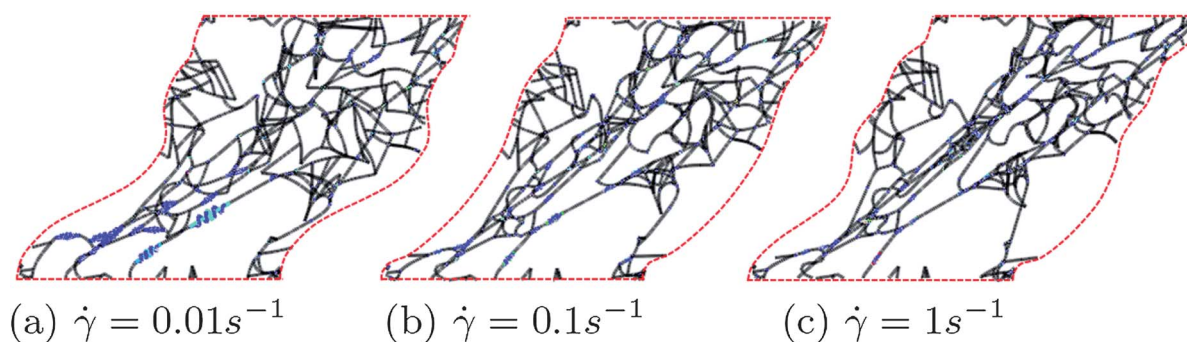


Fig. 2 Deformed configurations of the network in Fig. 1 experiencing a macroscopic shear strain of 50% under three different shear rates. Blue springs are dissociated crosslinks.

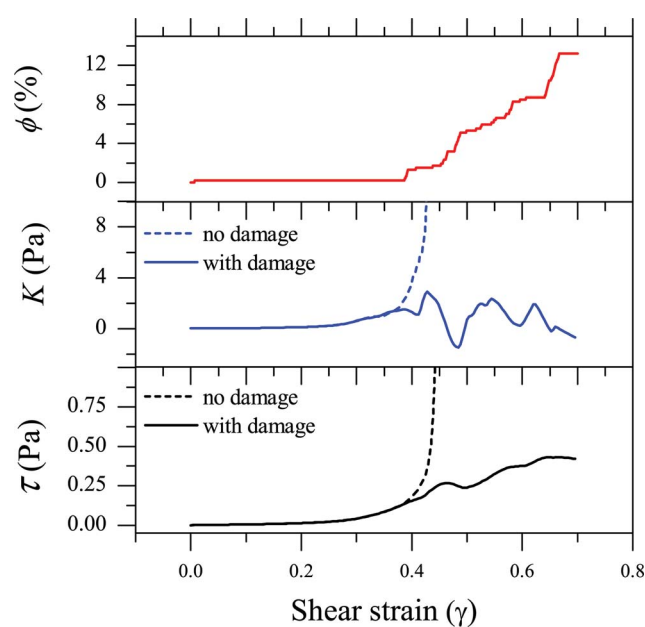


Fig. 3 Plot of stress, stiffness and damage as a function of strain for $\dot{\gamma} = 1 \text{ s}^{-1}$. The dotted curves indicate the response of pristine networks.

$$\phi(t) = \frac{\text{Number of crosslinks broken at time } t}{\text{Total initial number of crosslinks}} \quad (4)$$

3.1 Deterministic network response

Fig. 3 shows the evolution of the average shear stress τ , tangent shear stiffness $K = \partial\tau/\partial\gamma$ and damage fraction ϕ as a function of shear strain γ for the network in Fig. 1 subjected to $\dot{\gamma} = 1 \text{ s}^{-1}$. In the initial flimsy regime the stress is low owing to the low bending rigidity of the filaments and the low initial stiffness of the crosslinks. This is the regime of filament reorientation that aligns them along the principal stress directions. The damage is also low in this regime, which indicates that at this stage the lifetime of most of the crosslinks is larger than the time-scale associated with the imposed local strain rate.

At $\gamma \approx 0.2$ the stress begins to increase at a faster rate due to preferential alignment of some fraction of the filaments along the axis of principal tension together with the fact that the initially flimsy crosslinks get fully stretched to l_0 (eqn (3)) and lock. As

these filaments become taut, their stretching stiffness, which is orders of magnitude larger than the bending stiffness, comes into play and determines the overall network response.²¹ Consequently, the damage process also occurs faster because the larger forces experienced by the crosslinks dramatically reduce their lifetime (eqn (1)) resulting in an increased likelihood of satisfying the dissociation criterion. As damage develops, the average network stress and tangent stiffness increasingly deviate from their pristine counterparts (shown by the dotted curves). Although the stress continues to rise, the rate of increase slows down over a short strain range ($\gamma \approx 0.4\text{--}0.42$) that manifests as a *temporary* drop in the network stiffness. As the crosslink scission process starts dominating the response ($\gamma \approx 0.45$) the stiffness drops precipitously. The stress and stiffness do exhibit some recovery, which is due to reorganization of the intact crosslinked filaments into aligned bundles (stress fibers). It is worth noting that there may be situations where a network may soften temporarily, but it may not necessarily lead to a colossal loss of load carrying ability. This indicates a competition between the stiffening mechanism, driven by the tendency of a network to reorient the majority of the filaments along the principal tensile axis in order to maximize the stretching stiffness, and the scission-based softening mechanism. As long as there are a sufficient number of intact crosslinks, the overall system redundancy helps retain dominance of the stiffening process. Eventually, the softening mechanism prevails over the stiffening mechanism due to increasing force. In fact, to some extent, it is a self-cascading process. Each crosslink dissociation brings about an increased tendency of reorientation of the intact network filaments, because these filaments experience weaker constraint from their surroundings. This results in higher forces on the intact crosslinks, which further increases their probability of dissociating even more rapidly. Concomitantly, the damage evolves with strain rapidly beyond $\gamma \approx 0.5$ (Fig. 3).

We now discuss the rate-dependent mechanical response of the network. Fig. 4 shows evolution of the normalized tangent

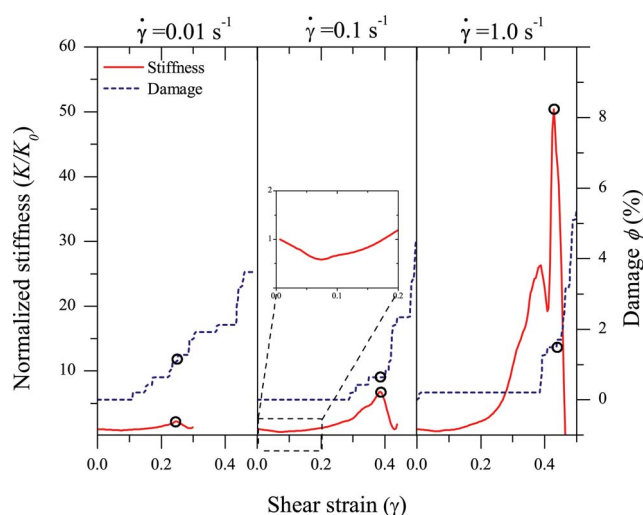


Fig. 4 Rate-dependent stiffness and damage evolution for three applied rates. Stiffness degradation of networks coincides with the rapid increase in the damage (marked by circles). Inset shows the softening regime at small strains due to filament buckling.

stiffness, K/K_0 (K_0 is the initial stiffness), and damage for the three shear rates. In each case, the network stiffness has an initial flimsy regime as depicted earlier in Fig. 3. It is evident that the network stiffness shows an initial gradual reduction, which exists even in the absence of crosslink scission, before it begins to increase (see inset in Fig. 4). This happens because filaments reorient toward the principal stress direction, a certain proportion experience tension while the remainder undergo compression. Given the high flexibility of filaments, compression induces buckling—a structural softening mechanism—which is not necessarily irreversible.^{21,31} Consequently, the entire stress is carried by the filaments under tension after they are fully taut. As noted in the preceding section, the filament straightening is concomitant with the nonlinear increase in the overall network stiffness. Importantly, Fig. 4 shows that the degree of nonlinear stiffening is rate-dependent. With increasing applied rate, the overall network response increases; higher stiffening and a higher peak before the loss of stiffness occurs. The rate-dependent stiffening and the peak stiffness are a direct result of the interaction between the loading rate and crosslink scission rate (eqn (1)). At slow strain rate the dissociation criterion (eqn (3)) is more likely to be satisfied even at small strains. Therefore, damage initiates early for lower $\dot{\gamma}$ and extends over the entire strain range up to the point of collapse. With increasing strain rate the damage initiates later, but it evolves more rapidly as can be deduced from the steeper jumps on the damage–strain curves. At higher applied strain rates the induced local rate may exceed the dissociation rate resulting in the crosslink not having sufficient time to break before the force has changed. Naturally, such a delay means that the network remains intact for larger strain values and, therefore, exhibits an overall higher stiffness at a given strain compared to those deformed at lower strain rates. Interestingly, this situation is akin to the dislocation kinetics in metals that exhibit rate-sensitivity at the elastic to plastic transition.⁵¹

Of the three shear rates considered here, the maximum peak normalized stiffness obtained is ~ 50 for $\dot{\gamma} = 1 \text{ s}^{-1}$ and the minimum is ~ 2 for $\dot{\gamma} = 0.01 \text{ s}^{-1}$. Soon after the point of maximum stiffness, the network collapses. We characterize this loss of structural functionality of the network by the *failure strain*, γ_f , at which the τ – γ curve crosses the K – γ curve (Fig. 3). Although the simulations may continue beyond this point, we consider γ_f as the measure of structural failure, because the subsequent stiffening effect is usually much weaker than the one before the colossal stiffness drop. From a microstructural viewpoint, at the failure strain there is a substantial deterioration of the network integrity brought about by scission of a critical fraction of the total crosslink population.

3.2 Stochastic network response

The results presented in the preceding section are for a fixed network topology with deterministic scission kinetics. However, there are at least two sources through which variability may arise in the responses, even in the case of fixed $\bar{\rho}$. First, it is evident from experiments that the crosslink scission is a stochastic process.^{42,43} Thus, at a given deformation rate, F_{cr} for crosslink scission may be scattered about a mean value. Second, one may be able to generate myriad topological realizations for a given

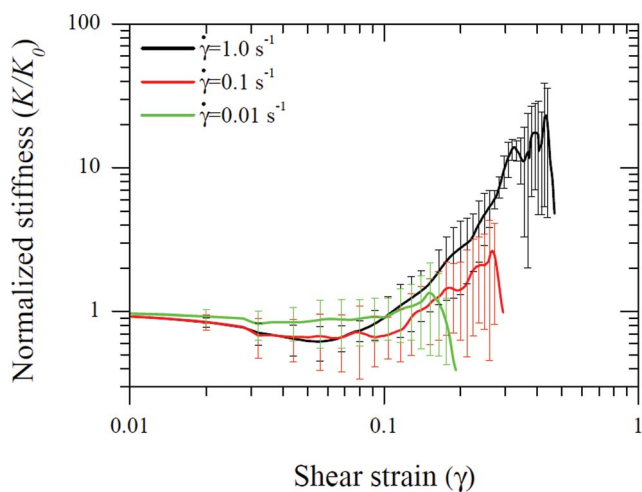


Fig. 5 Stochastic rate-dependent response of networks. Solid lines indicate mean response and error bars indicate one standard deviation.

orientation distribution function. In this section, we investigate the stochastic effects in the rate-dependent behavior of networks arising from these sources of variabilities. We consider five different realizations of the networks corresponding to $\bar{\rho} = 10$. For each realization, the stochastic nature of crosslink scission is captured through the KMC procedure (Section 2), which is invoked for every crosslink in a given network. The crosslinks are ranked in an ascending order of their lifetimes, t , and the one with the minimum lifetime, t_{\min} , is compared with the critical lifetime, \hat{t} . We perform five such simulations for each network realization. Thus, for a given $\dot{\gamma}$ we simulate twenty-five cases. We note in passing that the variability arising from the latter is also expected to depend on the size of the computational window, \mathcal{W} . A discussion about the topological variability due to the filament density and size of the computational window is presented in Appendix A.

Fig. 5 shows the network stiffness evolution with strain for three different applied strain rates. Each curve is an average of 25 simulations and the error bars indicate the variability due to the aforementioned sources of randomness. The responses indicate rate-sensitive stiffening and failure, but also exhibit significant variability as indicated by error bars. The variability is low at small strains ($\gamma \approx 0.05$), but it increases beyond that. Although not shown here, our simulations indicate that topological variations, which are mediated by the computational domain size, play a bigger role than the stochastic scission and some of this can be reduced by sampling larger regions (Appendix A). However, microstructural characteristics also mediate this variability. This is primarily due to the fact that as each network topology accrues damage due to crosslink scission, the local rearrangements of the filaments can vary significantly.

A quantitative comparison with experiments is challenging due to the large number of parameters involved: actin concentration, actin-ABP ratio, filament length, distance between crosslinks, rate of loading *etc.* Fig. 6 summarizes experimental data on the peak normalized network stiffness for F-actin networks crosslinked with various ABPs.^{15,18,28,52–54} It also superposes the present simulation results (square boxes with error bars). It should be noted, however, that the different

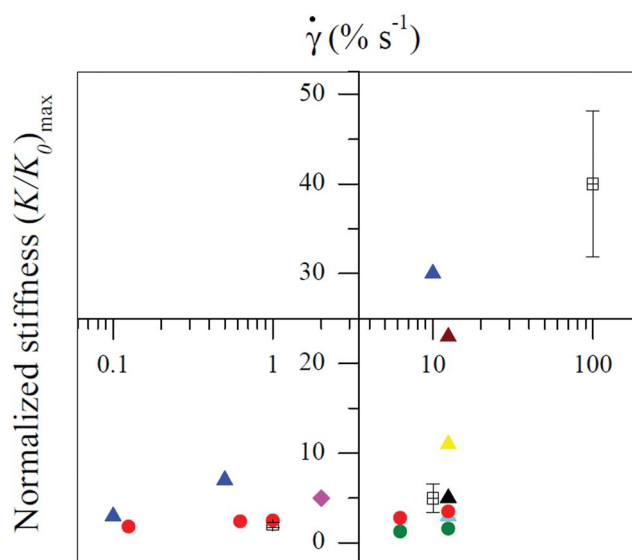


Fig. 6 Peak normalized stiffness obtained from experiment and the simulation results. The results shown above are for networks formed by various crosslinkers. Triangles correspond to the crosslinker filamin, circles are for fascin and diamonds for rigor heavy meromyosin (rigor-HMM) bonds. Colors indicate that the data is from different experiments.^{15,18,28,52–54} The present simulation results are shown by the rectangular boxes with error bars.

experimental results in the figure may not be directly comparable as the concentration of actin and ABP are not the same; also, the filament lengths may differ. For the data shown in Fig. 6, the concentration of F-actin varies from 0.4–0.8 mg ml⁻¹. The concentration ratio of ABP to actin varies from 0.003 to 0.01. The experimental result that compares well with our simulation results are from Kasza *et al.*⁵² (black triangle in Fig. 6), where the F-actin concentration is ~ 0.5 mg ml⁻¹ with $L \approx 10$ μ m, similar to the parameters used here.

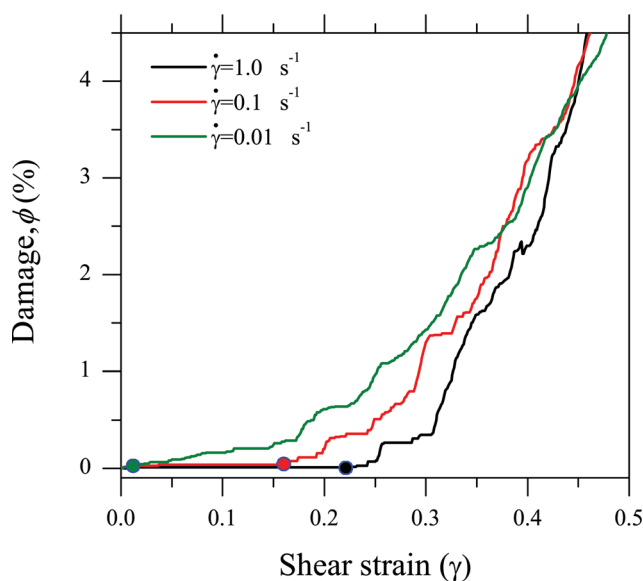


Fig. 7 Damage evolution for three applied shear rates. Each curve is an average of 25 simulations. The solid circle on each curve indicates incubation strain γ_{in} for that particular rate.

Fig. 7 shows the average rate-dependent evolution of the damage, ϕ , with strain corresponding to the stiffness evolution in Fig. 5. The trend is similar to the one in the deterministic simulations (Fig. 4) and given that this result stems from a sizable number of simulations, we identify two universal features: (a) incubation strain, γ_{in} , which characterizes the minimum macroscopic deformation that a network should accrue before crosslinks begin to dissociate, and (b) rate of growth, $\dot{\phi}$, beyond incubation. As can be noted, γ_{in} has a direct relationship with the applied rate: networks subjected to lower rates of loading possess a propensity to early initiation of damage, while at higher rates, damage initiation takes place only at large strains. Such information is not available in experimental literature as it may not be possible to isolate the damage incubation characteristics in an experiment. However, one may be able to reconcile it in an indirect fashion. In the works of Broedersz *et al.*⁵⁵ and Lieleg and Bausch,³³ for example, networks subjected to lower applied shear rates start to stiffen at higher strains compared to those sheared at higher rates. This could be attributed to the fact that the damage (crosslink scission) is more severe in the former, which implies lower incubation strain while the latter shows a delayed damage initiation *i.e.* higher incubation strain. Another interesting observation is that, irrespective of the applied rate, the damage evolution appears to converge to a single value of $\sim 4\%$ with $\gamma \approx 0.45$, beyond which a runaway growth occurs especially for higher strain rates.

Fig. 8a and b show the rate-dependent γ_{in} and the critical damage for stiffness collapse, ϕ_{cr} , with their corresponding variability. Whereas the former clearly indicates a rate-dependent behavior, the same cannot be said about the latter owing to a large scatter. Another important observation in the damage evolution process is that the ϕ_{cr} ranges between $\sim 0.5\%$ and 3% , while the loading rate and corresponding peak stiffness vary by three orders of magnitude. This low critical damage is ascribed to the non-affine nature of the network response. It can be observed from Fig. 8b that the variation in ϕ_{cr} is minimum for the shear rate $\dot{\gamma} = 0.1 \text{ s}^{-1}$. For the lower rates, crosslink scission is vigorous starting at a very small strain and for higher rates the crosslink scission is very rapid after incubation, which brings in substantial variability in ϕ_{cr} . Given that ϕ_{cr} is relatively rate insensitive, from

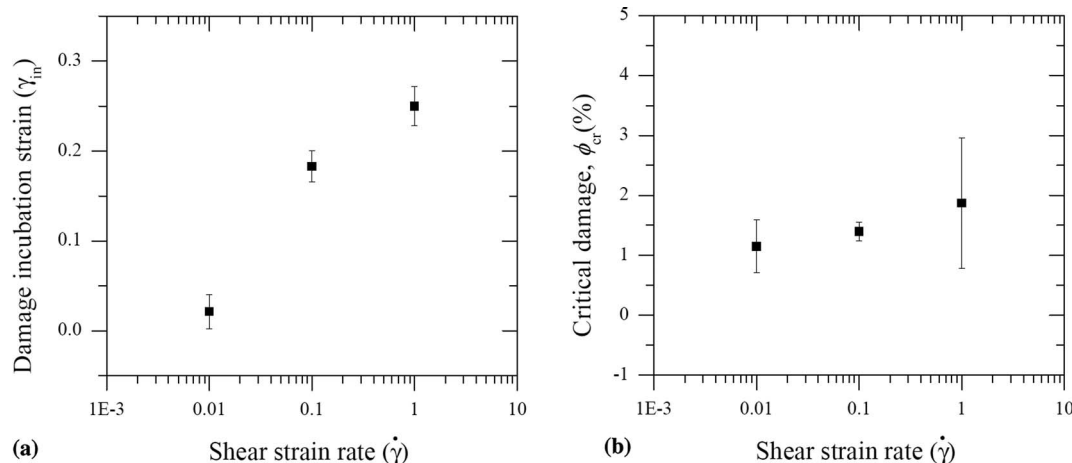


Fig. 8 Shear strain rate effects on damage incubation strain γ_{in} and critical damage ϕ_{cr} . (a) Damage incubation strain. (b) Critical damage for failure.

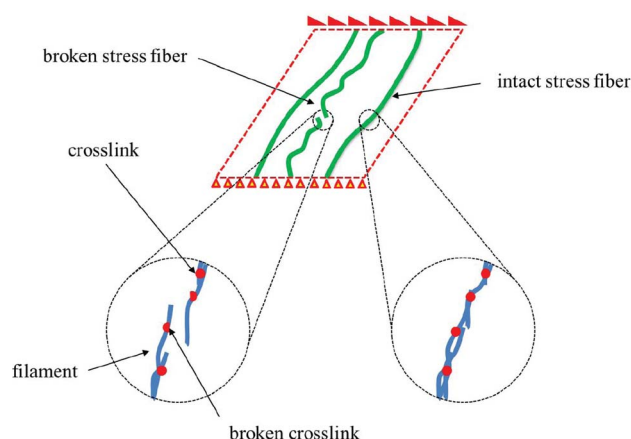


Fig. 9 Schematic showing the formation of stress fibers at large deformation due to the preferential alignment of the filaments along the loading direction and its failure due to crosslink scission. Scission of a small fraction of crosslinks may result in the failure of stress fibers which in turn results in the network failure. The view on the left shows a broken stress fiber and the right view shows the intact one.

a variability consideration, one may posit that there is an optimum rate that provides more deterministic information about critical damage irrespective of the computational window size. At the point where the network collapses, the main load-carrying components are the filaments that have already aligned in the principal tensile direction. In this scenario, although there may be several intact crosslinks that connect the filaments, the effective system redundancy is governed by stress fibers. These stress fibers are like a system of springs in parallel where each of the stress fibers comprises several filament-spring combinations connected in series, supporting the applied deformation. When one crosslink within any of these stress fibers dissociates, it corresponds to loss of an entire stress fiber thereby reducing the effective stiffness dramatically (Fig. 9). In other words, rearrangement of filaments lowers the effective redundancy of the network, which would otherwise help maintain its structural integrity over a larger deformation.

4 A continuum model with damage

In this section, we present a phenomenological, homogenized continuum model that incorporates the effect of non-affinity and deformation-induced damage evolution due to crosslink scission. The main objective is to show that the damage kinetics can be introduced within an existing homogenized model and to demonstrate that such an enriched model qualitatively mimics the DN simulation results.⁵⁶ The model is based on the work of Planas *et al.*⁵⁷ that accounts for the filament orientation evolution in an average sense, but unlike their work that ignores non-affine effects, we approximately incorporate the influence of non-affine deformations.⁵⁸

4.1 Affine deformation model

F-actin filaments crosslinked by ABPs are assumed to be uniformly distributed in the unloaded configuration.⁵⁹ Filaments are assumed to be isotropic and homogeneous with crosslinks at the end points. The initial filament orientation θ is accounted for using a distribution function. A uniform probability density function for a continuous distribution is given by⁵⁷

$$\Gamma(\mathbf{x}) = \begin{cases} \frac{1}{b-a} & \text{if } a \leq \theta \leq b \\ 0 & \text{if } \theta < a \text{ or } \theta > b \end{cases} \quad (5)$$

where a and b denote the limits of θ . In the present 2D scenario with $0 \leq \theta \leq \pi$ the initial spatial distribution function is given by⁵⁷

$$\Gamma(\mathbf{n}, \mathbf{x}) = \frac{f_f}{2\pi} \quad (6)$$

where f_f is the volume fraction of the filaments. In this homogenized theory, information about $\bar{\rho}$ is embedded through f_f . For the 2D case, we equivalently define it as the area fraction, *i.e.* $f_f \approx NLd/W^2 = 0.007$ where d is the diameter of filaments. \mathbf{n} is the unit vector in the reference configuration \mathbf{x} , where the filament distribution is uniform, and is given by

$$\mathbf{n} = \mathbf{e}_1 \cos \theta + \mathbf{e}_2 \sin \theta. \quad (7)$$

where \mathbf{e}_1 and \mathbf{e}_2 are unit vectors in Cartesian coordinates. During deformation, filaments continually align with the loading direction and the overall orientation distribution deviates from its initial uniform state.

Consider a filament connected with two crosslinks in series. The stress in this filament–crosslink system is described by

$$s_f(\lambda) = E_f^\lambda (\lambda - 1) \quad (8)$$

where λ is the axial stretch in this system. E_f^λ is the *equivalent* elastic modulus of the filament–crosslink system, ignoring the non-affine and damage effects. Note that E_f^λ may itself be a function of λ depending upon the constitutive behaviors of the filament and the crosslinks. At any time t , a macroscopic simple shear γ ($= \dot{\gamma}t$) applied to the network results in the following deformation gradient.

$$\mathbf{F} = \begin{bmatrix} 1 & \gamma \\ 0 & 1 \end{bmatrix} \quad (9)$$

With the affine deformation assumption, the stretch, λ , in an individual filament–crosslink system due to γ is⁵⁷

$$\lambda(\theta) = |\mathbf{F}\mathbf{n}| = \sqrt{1 + \gamma^2 \sin^2 \theta + 2\gamma \sin \theta \cos \theta} \quad (10)$$

and the corresponding Cauchy stress (in 2D) is

$$\boldsymbol{\sigma} = \int_0^\pi s_f(\lambda) \left[\frac{\mathbf{F}\mathbf{n} \otimes \mathbf{F}\mathbf{n}}{|\mathbf{F}\mathbf{n}|} - \frac{1}{2} |\mathbf{F}\mathbf{n}| \mathbf{I} \right] \Gamma(\mathbf{n}, \mathbf{x}) d\theta - p \mathbf{I} \quad (11)$$

where \otimes denotes a tensor product, \mathbf{I} is the identity tensor and $|\mathbf{a}|$ indicates the magnitude of a vector \mathbf{a} . To account for the effect of all the filaments, eqn (11) is integrated over the entire range of angles considered. For an initial uniform distribution, filaments are present in all orientations and eqn (11) becomes

$$\boldsymbol{\sigma} = -p \mathbf{I} + \int_0^\pi \frac{E_f^\lambda f_f}{\pi} \left\{ \mathbf{F}\mathbf{n} \otimes \mathbf{F}\mathbf{n} - \frac{1}{2} |\mathbf{F}\mathbf{n}|^2 \mathbf{I} \frac{\mathbf{F}\mathbf{n} \otimes \mathbf{F}\mathbf{n}}{|\mathbf{F}\mathbf{n}|} + \frac{1}{2} |\mathbf{F}\mathbf{n}| \mathbf{I} \right\} d\theta. \quad (12)$$

In determining the equivalent modulus E_f^λ , the filaments are modeled as linearly elastic while the crosslinks are assumed to follow worm-like chain (WLC)-model.^{16,60} With this, E_f^λ in eqn (12) becomes

$$E_f^\lambda = \frac{K_f L}{A} \left(\frac{\hat{\lambda}^{-3}}{2} + 1 \right) \quad (13)$$

$$1 + \frac{\hat{\lambda}^{-3}}{2} + \frac{2K_f l_0 l_p}{k_B T}$$

where $\hat{\lambda} = (1 - (\lambda - 1))$, and K_f and A are the stiffness and area of the filaments, respectively.

As discussed later, the initial response is determined by the crosslink behavior as it is the more compliant of the two. However, gradually, as the macroscopic strain increases, the crosslink stiffens and the filament starts playing a dominant role. This is further aided by the filament reorientation process.

4.2 Effect of non-affinity

The simple springs-in-series model describing E_f^λ leads to affine deformations, whereas a network may deform in a non-affine manner triggered by filament bending.^{26,61} In this work, we do not attempt to rigorously formulate this effect. However, it is important to account for it and, to that end, we refer to the work of Zaccone and Scossa-Romano⁵⁸ who elegantly showed that in amorphous solids,

$$\mu = \mu^A - \mu^{NA} = \mu^A (1 - z') \quad (14)$$

where μ is the actual network shear modulus, μ^A is the modulus assuming affine deformations while μ^{NA} is the non-affine contribution that softens the overall response. In other words, the term inside the bracket describes the magnitude of non-affinity through z' that is related to the coordination number indicating nearest neighbor particles in contact and dimensionality of the problem. While eqn (14) is only valid for central force systems, it is used here as guidance for writing a similar form for biopolymeric networks where bending energy can stabilize the floppy (soft) modes.^{62,63} Motivated by the elegance of eqn (14), we write

$$E_r = E_r^\lambda (1 - \zeta_0) \quad (15)$$

where ζ_0 is a dimensionless quantity (<1) that characterizes the network non-affinity induced by bending deformations. For a given filament density, it is expected to depend on an effective coordination number, \bar{z} , at a crosslink (determined by whether it is an X, an L or a T type junction),^{64,65} the effective filament length, l_c , between the crosslinks and a length-scale, λ , describing the propensity of a filament to bending.^{26,66} Although not derived here in detail, we suggest that ζ_0 would be directly proportional to l_c , but would depend inversely on \bar{z} and λ . Finally, using continuum damage mechanics, we superpose the effect of scission-induced damage and write the effective elastic modulus, E_e , of the filament–crosslink system as

$$E_e = E_r^\lambda (1 - \zeta_0 - \zeta_1 \phi) \quad (16)$$

where ζ_1 is a phenomenological sensitivity parameter that accounts for the effect of enhancement of degradation due to reduced redundancy of the network as stress fibers form (Fig. 9). Eqn (16) indicates that the softening of the network brought about by bending induced non-affinity (characterized by ζ_0) is accentuated by the damage induced from crosslink scission. The modulus E_r^λ in eqn (12) is substituted by eqn (16). The resulting expressions for the network stress components are complicated functions of γ and are solved using MAPLE® to obtain the overall differential shear stiffness.

4.3 Damage evolution

Reiterating the characteristic features of damage evolution, we have rate-dependent incubation strain and damage growth but a rate-independent strain, $\gamma_e \approx 0.45$, at which the runaway damage growth occurs. From these characteristics we propose the following evolution law for the crosslink scission fraction

$$\dot{\phi} = \begin{cases} 0 & \text{if } \gamma \leq \gamma_{in} \\ \dot{\phi}_0 \left(\frac{\dot{\gamma}}{\dot{\gamma}_0} \right) \left(\frac{\gamma}{\gamma_e - \gamma} \right)^n & \text{if } \gamma > \gamma_{in} \end{cases} \quad (17)$$

where $\dot{\phi}_0$ is the characteristic scission rate obtained at a characteristic macroscopic deformation rate, $\dot{\gamma}_0$, and n indicates its dependence on the applied and runaway strains. In the equation, the rate-dependent incubation strain, $\gamma_{in} = \alpha(\dot{\gamma}/\dot{\gamma}_0)^p$, is characterized by the parameters α and p . Damage evolves only after γ_{in} is reached. These parameters are obtained from the damage evolution curves (Fig. 7) and the values are given in Table 1.

4.4 Network response: continuum modeling results

Fig. 10 shows the rate-dependent stiffness and damage evolution with macroscopic shear strain obtained from the homogenized model. The result reproduces qualitative trends that were obtained from the DN results (Fig. 4). As both the crosslink and the filament

Table 1 Constituent parameters used in the continuum model

α	p	$\dot{\phi}_0$ (s ⁻¹)	$\dot{\gamma}_0$ (s ⁻¹)	γ_e	n	ζ_0	ζ_1
0.25	0.4	0.067	1	0.45	0.4	0.8	50

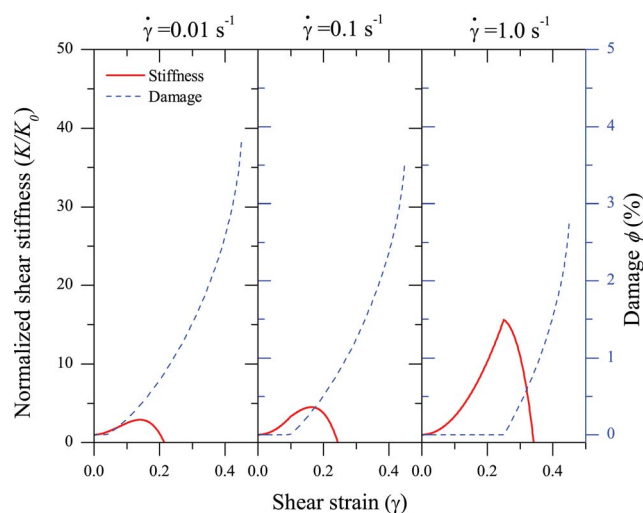


Fig. 10 Rate-dependent stiffness response of the network from the homogenized model.

are connected in series, at small strains the response is mediated by the crosslink due to low stiffness. With continued deformation the crosslink stiffens and the filament starts contributing to the overall stiffness, because it now assumes the role of the weakest link in the filament–crosslink series system. Yet, the network stiffness increases by several orders of magnitude owing to the reasonably large stretching stiffness of the filament.

Using the parameters in Table 1, the peak stiffness values obtained are in the same range as those obtained from experimental observation⁵² and our DN model. Importantly, the underlying microstructural evolution, damage evolution and the resulting rate sensitivity of the biopolymer networks are captured using the current model in an average sense without the necessity to delve into the specifics of a given network. The microstructural evolution of a network through filament reorientation causes stiffening of the overall response. In the model of Planas *et al.*,⁵⁷ the current average network orientation without considering the damage is described by β as

$$\beta(\mathbf{x}) = \frac{1}{\pi} \int_0^\pi \frac{\cos \theta + \gamma \sin \theta}{|\mathbf{F}\mathbf{n}|} d\theta, \quad (18)$$

i.e. β is the ratio of the projected length of filaments on the reference axis to the total length of the filaments. Evolution of β depends on the type of deformation and the reference axis. Fig. 11 shows the process of filament reorientation in a network, obtained by numerically integrating eqn (18) for the simple shear case. For simple shear deformation, the initial principal axes are at $\sim 45^\circ$. During deformation, filaments get oriented towards the principal axes. The reference axis considered for the calculation of β remains fixed at 45° while the principal axis for the simple shear case start with 45° and tends towards 0° at very large strains. For a 2D uniform distribution, the initial value of β is $2/\pi$ and the limiting value when θ tends to be 0° is $1/\sqrt{2}$ (not shown in Fig. 11). For the uniform distribution, filaments are oriented in all directions in the undeformed state, but during deformation they tend to be oriented to 45° at small strains, reflected as initial increase in β , and then progressively to 0° , reflected as the drop in β .

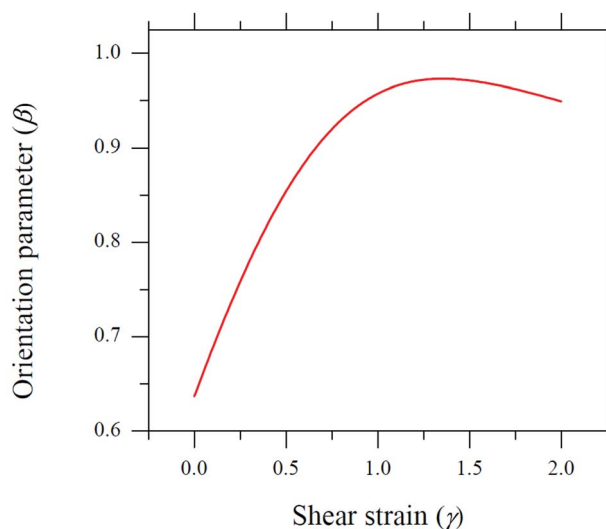


Fig. 11 Evolution of filament orientation for shear loading with respect to the 45° axis. At small strains, the principal loading direction coincides with the 45° axis and later it deviates, evident from the initial increase and then decrease in the orientation parameter.

Although not explored here, another important feature of this model is that the variability in the damage evolution could be incorporated into the continuum model by adopting distribution functions for the parameters in Table 1, as those are based on the variability obtained from the DN calculations. In such a scenario, the values in Table 1 could be mean values.

5 Conclusions

In this work, we developed microstructurally informed models to gain insights into the rate-dependent mechanical behavior of soft, fibrous networks. An F-actin network crosslinked with filamin was chosen as a model system for this investigation. The DN approach was enriched with crosslink scission kinetics, which renders the response rate-sensitive. The stochastic nature of the scission process is embedded in the approach by integrating a KMC procedure into the FE framework. We addressed the variability of responses that arise from sampling effects, which enabled us to understand statistical aspects of the network mechanics. We also developed a homogenized damage model that was merged with an existing continuum model and phenomenologically accounted for network non-affinity. Although not explored here, an important feature of this homogenized model is that the variability in the scission-induced damage could be incorporated in a seamless manner by adopting distribution functions for the parameters in its evolution function.

In this work, the sole mechanism for rate-dependent behavior is rate-dependent damage evolution. Factors such as viscoelasticity, reformation of crosslinks and active rearrangement of the network architectures are not accounted for. Another mechanism which is not accounted for is the strain-rate hardening of crosslinks.⁴¹ In the case of a strain-rate hardening type of crosslink, both γ_f and peak stiffness could be modulated due to the higher forces experienced by the crosslink. It is seen that the

mechanical response is inextricably linked to topological factors such as filament density, crosslink density and network architecture.⁶⁵ The dependency on the last factor is not well understood and strong connections have to be made between the topology and mechanical response to fully understand behaviors of filamentous networks. The results presented here are based on 2D filamentous networks whereas real biopolymeric networks are three-dimensional. The lower constraint effect offered by the latter^{27,37} and the resulting extended non-affinity may affect the damage evolution quantitatively, although the qualitative behavior should still hold. Finally, we have not addressed the role of the fluid medium that surrounds these networks. To the lowest order, this will result in a shear stress that varies linearly with the strain rate, with solvent viscosity being the proportionality constant. This may be effectively construed as dashpots embedded within the network and this may also influence the damage evolution, especially if the viscous time-scales compare with the dissociation time-scales and applied loading rate.

The research problem addressed in this paper lies at the nexus of mechanics and chemistry. A broad class of phenomena in cellular and molecular biophysics are in this arena, including force induced unfolding or conformational change of proteins, force induced activation of ion channels, chemical to mechanical energy conversion in muscles and polymerization-induced force generation in actin filaments.⁶⁷ In all these problems, the effect of force on equilibria and rates of chemical reactions is treated using variants of the Bell and Eyring models at the level of single molecules or single fibers. Our treatment of the breaking of crosslinks follows along these lines but we have gone further by constructing a damage model at the continuum level that is informed by thermal activation theories at the scale of single crosslinks. As such, our evolution laws are written for tensorial quantities such as stresses and strains (not just forces or extensions) even though they have their origins in one-dimensional ideas at the single molecule level. We expect that our methods that combine deterministic and stochastic elements will be applicable to a variety of filamentous network architectures where there is continuous interplay of mechanical and chemical forces.

Appendices

A Topological variability

The issue of sampling size is important in constructing artificial microstructures. For example, from the viewpoint of computational cost it may not be possible to simulate large-scale specimens (Fig. 12). Instead, one may need to choose smaller windows from the large specimen. While on an average, such a windowing procedure is expected to retain global features of the larger architecture, *e.g.* filament and crosslink density, the local details could vary significantly as shown in Fig. 12. In turn, this variability in the local architectures is deemed to influence the mechanical responses. We briefly discuss these statistical aspects with reference to the topological isotropy as a function of computational window size, W , and filament density, $\bar{\rho}$.

To begin with, we assumed a uniform filament distribution for a given window size, W , and placed the filaments randomly in the

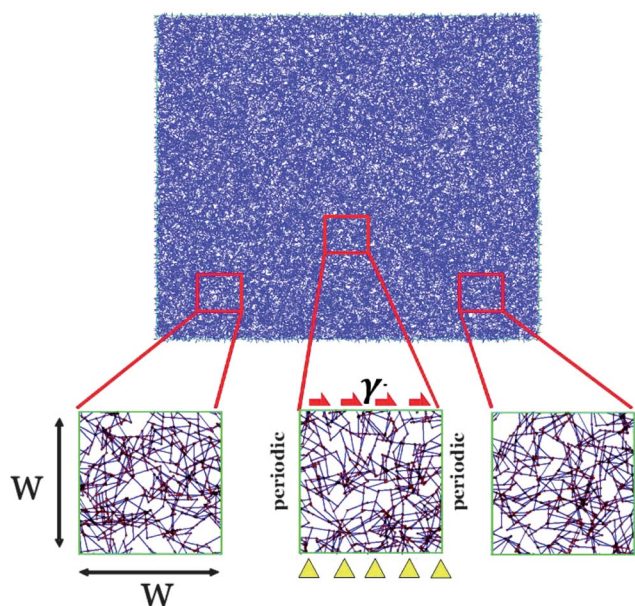
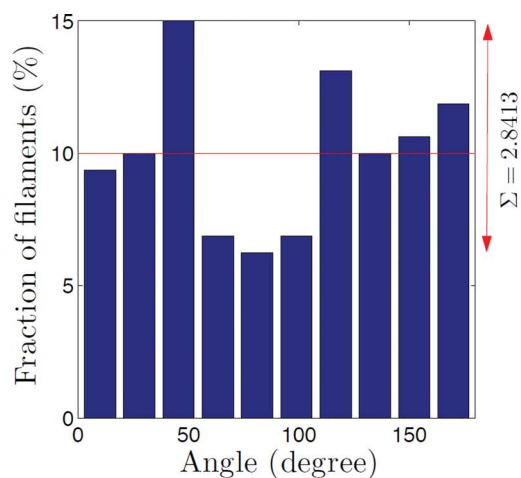
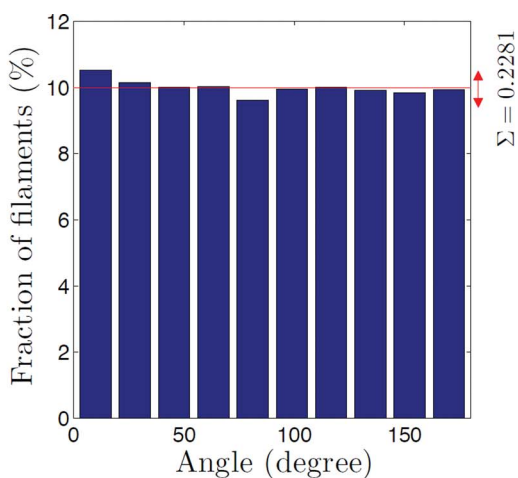


Fig. 12 Idealization of the actual network by smaller computational windows. Depending on the location, filament distribution inside windows could be different. Though nominal network parameters like $\bar{\rho}$ and number of crosslinks are the same, responses could vary for different filament realizations.

window until the desired $\bar{\rho}$ was obtained. In order to quantify the filament orientation distribution of a given network, filaments were grouped into ten bins of orientations ranging from 0° to 180° with each bin of width 18° . The number of filaments in each bin was normalized by the total number of filaments and this filament fraction was used in rest of the calculations. For a given $\bar{\rho}$ or W , we considered five network realizations to obtain the average, ξ , and the standard deviation, Σ , of the filament fraction. Given that the range of angles considered was from 0° to 180° and the distribution was uniform, the average value is always $\sim 10\%$ and we calculated the coefficient of variation



(a) $W = 40 \times 40 \mu\text{m}$



(b) $W = 1000 \times 1000 \mu\text{m}$

Fig. 13 Filament distribution with $\bar{\rho} = 10$ for two window sizes, W , are shown with the mean (red line) and standard deviation. As the W increases, the distribution becomes more uniform.

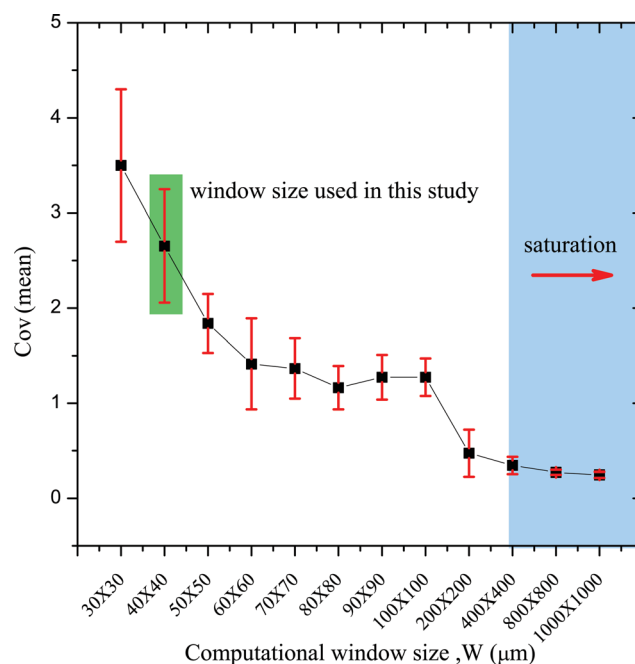


Fig. 14 Variability in filament distribution decreases as the W increases. Increasing the W beyond $200 \times 200 \mu\text{m}$ does not reduce the variability in filament distribution.

($C_{ov} = \Sigma/\xi$). In the following sections, we discuss the statistical aspects arising from computational window size, W , and filament density, $\bar{\rho}$.

A.1 Increasing the computational window size. One of the approaches to get the idealized uniformly distributed filament networks is to increase the W for a given $\bar{\rho}$. We considered a case with $\bar{\rho} = 10$ and increased the window size, W , to find the optimum size at which the filament distribution becomes uniform. Starting with a W of $30 \mu\text{m}$, networks were generated with uniform filament distribution and filaments of length $L = 10$

μ and the largest W was 1000 μm (Fig. 13). As the W increases, distributions tend to be more uniform, reflected as a drop in the value of Σ .

Fig. 14 gives a summary of the parametric study with W ranging from 30 μm to 1000 μm . From the μ and Σ of each realization, C_{ov} was calculated. Using the C_{ov} of five realizations for a given W , μ and Σ of the C_{ov} of each W were calculated. From the limited number of realizations considered here, we deduce that the variability is very high when the W is 30 μm and there is a limitation for the lowest value for W that can be considered due to the fixed filament length of 10 μm and the rigidity percolation requirement. It can be noted that increasing W beyond 200 μm does not yield any substantial increase in the convergence of numerical approximations of uniform distributions (shown by the blue zone in Fig. 14). Increasing W is offset by the cost of computation. From a computational cost stand point, for a given $\bar{\rho}$, it would be necessary to consider a large number of realizations to obtain accurate bounds on the response variability, if one chose to use small W . For the present work, we chose 25 realizations to obtain the variability due to topological effects. The accuracy could be further improved with more realizations. The value of W used in the current study is marked in Fig. 14.

A.2 Increasing filament density. An allied question that arises is: how would $\bar{\rho}$ affect the variability if W is fixed. As the filament location and orientation are randomly generated, the greater the number of filaments, the better the chance of approximating the prescribed distribution function. Fig. 15 shows the filament distribution for two typical realizations with limiting values of $\bar{\rho}$. At $\bar{\rho} = 10$, the distribution shows large variability and the standard deviation, Σ , is high. As $\bar{\rho}$ increases, the distribution becomes more uniform and the standard deviation drops by an order of magnitude, but only at the very high filament density of $\bar{\rho} = 8000$. However, this is a reasonable choice only if the global responses also tend to be independent of $\bar{\rho}$, *e.g.* in networks mimicking highly crosslinked synthetic polymers. In problems

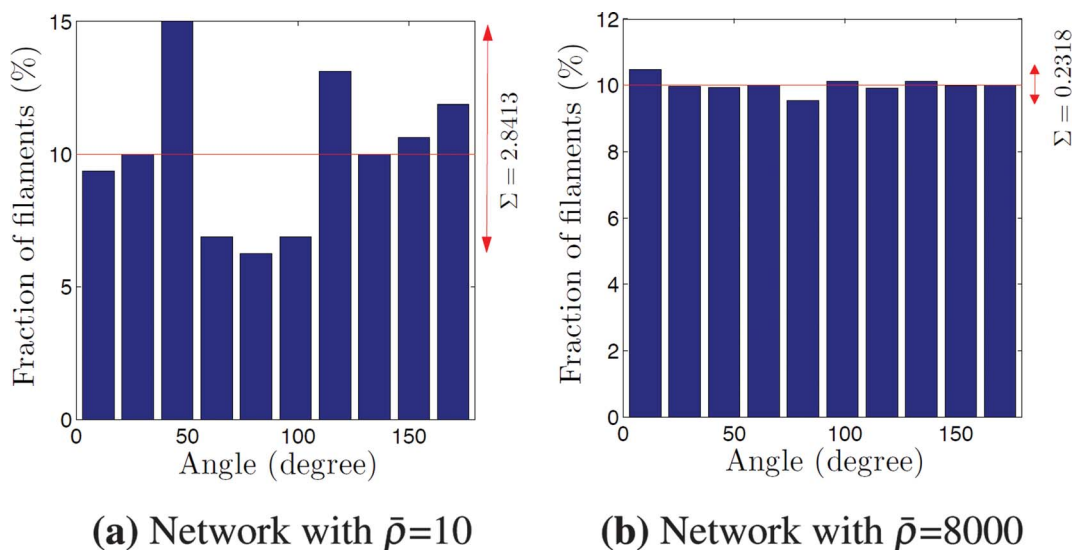


Fig. 15 The filament distribution for $\bar{\rho} = 10$ and 8000 is shown with the mean (red line) and standard deviation. As $\bar{\rho}$ increases the distribution becomes more uniform. W remains fixed at $40 \times 40 \mu\text{m}$.

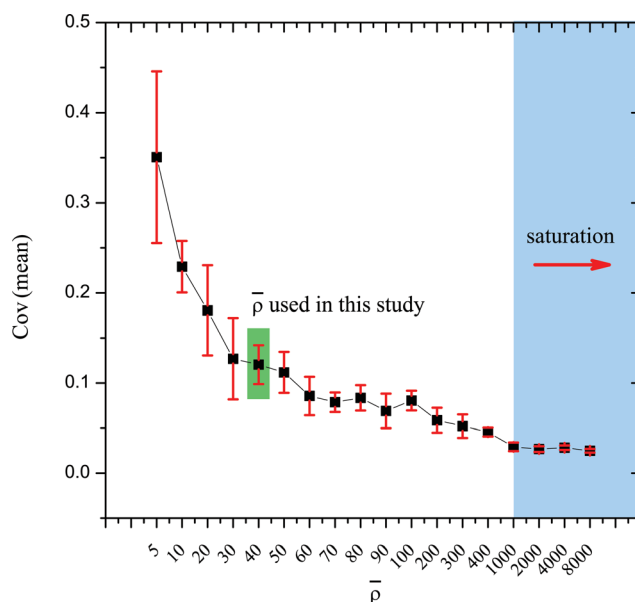


Fig. 16 Variability in the filament distribution decreases as $\bar{\rho}$ increases. Increasing $\bar{\rho}$ above 1000 brings no change in filament distribution.

concerning low density networks, *e.g.* biopolymers, increasing $\bar{\rho}$ would not be a natural option, because the responses tend to be a strong function of $\bar{\rho}$. In such cases, using reasonably large W with fewer realizations or small W with a large number of realizations would be the options. To find a good choice of $\bar{\rho}$ for a given $W = 40 \mu\text{m}$, so that the filament distribution approaches theoretical uniform distribution, networks were generated with $\bar{\rho}$ ranging from 5 to 8000 and five different realizations for each $\bar{\rho}$. Using the similar procedure as in Section A.1, Fig. 16 shows the variability of C_{ov} with $\bar{\rho}$, for a fixed W . It shows that C_{ov} decreases as $\bar{\rho}$ increases and that there is a saturation value; the blue zone shown in Fig. 16. Increasing $\bar{\rho}$ beyond 1000 does not change the distribution any further. It implies that multiple realizations of networks with $\bar{\rho} \geq 400$ would tend to yield nearly

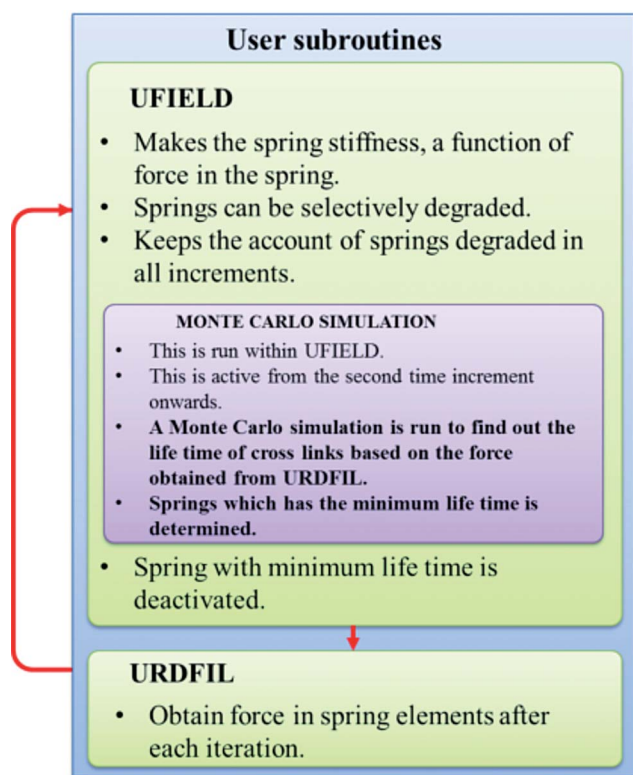


Fig. 17 Implementation of the crosslink scission algorithm within ABAQUS®.

identical global responses. Therefore, it seems that the variability arising from topological differences can be mitigated by choosing a $\bar{\rho}$ for a given W .

B KMC algorithm and implementation in finite element model

In bio- as well as synthetic-polymeric networks the length-scales of interest introduce stochastic effects due to the presence of thermal energy that superposes the mechanical energy. The KMC algorithm implemented in this work addresses this stochastic nature as a first-order reaction. This description is appropriate for an ensemble of similar bonds whose kinetics can be modeled deterministically by a first order ordinary differential equation (ODE) even though the breaking of each bond is a stochastic process. In particular, the probability density function corresponding to the time required to break the j^{th} bond can be written as

$$p_j(t) = k_j e^{-k_j t} \quad (\text{A1})$$

where k_j is dissociation rate of a bond and is given by eqn (1). Dissociation of crosslinks is based on the criterion given in eqn (3). In our FE implementation within ABAQUS®, we used a random seed that depends on the physical time at which the simulation was performed. This largely ensured that, for a given network topology, no two sequences of random numbers were identical.

Fig. 17 shows the schematic implementation of this procedure within ABAQUS®. Specifically, we wrote two user subroutines, which determine the kinetics of each crosslink modeled as

a bi-linear spring: (a) UFIELD to incorporate the Bell model that gives a crosslink dissociation rate—using this subroutine, we related the crosslink stiffness as a function of an appropriate field variable (axial force, F , in a crosslink)—and (b) URDFIL: to enable reading and storing those field variables for each crosslink so that they can be used by UFIELD.

Acknowledgements

SPJ acknowledges financial support through NUS AcRF Tier 1 Grant number R-265-000-339-112. ASA acknowledges financial support through NUS research scholarship. PKP acknowledges partial support through an NSF CAREER award grant number NSF CMMI-0953548.

References

- 1 M. Malkoch, R. Vestberg, N. Gupta, L. Mespouille, P. Dubois, A. Mason, J. Hedrick, Q. Liao, C. Frank and K. Kingsbury, *Chem. Commun.*, 2006, 2774–2776.
- 2 L. Hu, D. Hecht and G. Grüner, *Nano Lett.*, 2004, **4**, 2513–2517.
- 3 M. Gardel, J. Shin, F. MacKintosh, L. Mahadevan, P. Matsudaira and D. Weitz, *Science*, 2004, **304**, 1301.
- 4 L. Treloar, *The Physics of Rubber Elasticity*, Oxford University Press, USA, 2005.
- 5 R. HAgglund and P. Isaksson, *Int. J. Solids Struct.*, 2008, **45**, 868–878.
- 6 P. LeDuc and D. Robinson, *Adv. Mater.*, 2007, **19**, 3761–3770.
- 7 E. Chhabra and H. Higgs, *Nat. Cell Biol.*, 2007, **9**, 1110–1121.
- 8 T. Stossel, J. Condeelis, L. Cooley, J. Hartwig, A. Noegel, M. Schleicher and S. Shapiro, *Nat. Rev. Mol. Cell Biol.*, 2001, **2**, 138–145.
- 9 S. Suresh, *Acta Mater.*, 2007, **55**, 3989–4014.
- 10 A. Clark and E. Paluch, *Cell Cycle in Development*, 2011, pp. 31–73.
- 11 J. Sanger, *Proc. Natl. Acad. Sci. U. S. A.*, 1975, **72**, 1913.
- 12 J. Theriot and T. Mitchison, *Nature*, 1991, **352**, 126–131.
- 13 S. Hutchens, A. Needleman and J. Greer, *Appl. Phys. Lett.*, 2012, **100**, 121910.
- 14 S. Cranford and M. Buehler, *Nanotechnol., Sci. Appl.*, 2010, **3**, 127–148.
- 15 O. Lieleg, M. Claessens, Y. Luan and A. Bausch, *Phys. Rev. Lett.*, 2008, **101**, 108101.
- 16 C. Broedersz, C. Storm and F. MacKintosh, *Phys. Rev. Lett.*, 2008, **101**, 118103.
- 17 M. Gardel, F. Nakamura, J. Hartwig, J. Crocker, T. Stossel and D. Weitz, *Phys. Rev. Lett.*, 2006, **96**, 88102.
- 18 K. Schmoller, O. Lieleg and A. Bausch, *Biophys. J.*, 2009, **97**, 83–89.
- 19 O. Lieleg, M. Claessens and A. Bausch, *Soft Matter*, 2010, **6**, 218–225.
- 20 B. Schnurr, F. Gittes, F. MacKintosh and C. Schmidt, *Macromolecules*, 1997, **30**, 7781–7792.
- 21 P. Onck, T. Koeman, T. Van Dillen and E. Van Der Giessen, *Phys. Rev. Lett.*, 2005, **95**, 178102.
- 22 E. Huisman, T. Van Dillen, P. Onck and E. Van der Giessen, *Phys. Rev. Lett.*, 2007, **99**, 208103.
- 23 F. MacKintosh, J. Käs and P. Janmey, *Phys. Rev. Lett.*, 1995, **75**, 4425–4428.
- 24 F. Gittes and F. MacKintosh, *Phys. Rev. E: Stat. Phys., Plasmas, Fluids, Relat. Interdiscip. Top.*, 1998, **58**, 1241–1244.
- 25 K. Kasza, G. Koenderink, Y. Lin, C. Broedersz, W. Messner, F. Nakamura, T. Stossel, F. MacKintosh and D. Weitz, *Phys. Rev. E: Stat., Nonlinear, Soft Matter Phys.*, 2009, **79**, 041928.
- 26 D. Head, A. Levine and F. MacKintosh, *Phys. Rev. E: Stat., Nonlinear, Soft Matter Phys.*, 2003, **68**, 061907.
- 27 T. Van Dillen, P. Onck and E. Van der Giessen, *J. Mech. Phys. Solids*, 2008, **56**, 2240–2264.
- 28 C. Broedersz, K. Kasza, L. Jawerth, S. Münster, D. Weitz and F. MacKintosh, *Soft Matter*, 2010, **6**, 4120–4127.
- 29 Y. Termonia, *Pergamon Materials Series*, 2000, **4**, 271–291.
- 30 P. Chen and V. Shenoy, *Soft Matter*, 2011, **7**, 355–358.
- 31 O. Chaudhuri, S. Parekh and D. Fletcher, *Nature*, 2007, **445**, 295.
- 32 S. Tianxiang and P. K. Purohit, *Soft Matter*, 2012, **8**, 4664–4674.

- 33 O. Lieleg and A. Bausch, *Phys. Rev. Lett.*, 2007, **99**, 158105.
- 34 B. DiDonna and A. Levine, *Phys. Rev. E: Stat., Nonlinear, Soft Matter Phys.*, 2007, **75**, 041909.
- 35 M. Nunnally, L. Powell and S. Craig, *J. Biol. Chem.*, 1981, **256**, 2083.
- 36 A. Ott, M. Magnasco, A. Simon and A. Libchaber, *Phys. Rev. E: Stat. Phys., Plasmas, Fluids, Relat. Interdiscip. Top.*, 1993, **48**, 1642–1645.
- 37 E. Huisman, T. Van Dillen, P. Onck and E. Van der Giessen, *Phys. Rev. Lett.*, 2007, **99**, 208103.
- 38 S. Inc., ABAQUS Version 6.9 Online Documentation, 2010.
- 39 J. Condeelis, M. Vahey, J. Carboni, J. DeMey and S. Ogihara, *J. Cell Biol.*, 1984, **99**, 119s.
- 40 M. Jhon and D. Chrzan, *J. Mech. Behav. Biomed. Mater.*, 2009, **2**, 603–606.
- 41 M. Li and M. Kouza, *J. Chem. Phys.*, 2009, **130**, 145102.
- 42 M. Schlierf and M. Rief, *Biophys. J.*, 2006, **90**, L33–L35.
- 43 J. Ferrer, H. Lee, J. Chen, B. Pelz, F. Nakamura, R. Kamm and M. Lang, *Proc. Natl. Acad. Sci. U. S. A.*, 2008, **105**, 9221.
- 44 G. Bell, *Science*, 1978, **200**, 618.
- 45 A. Voter, *Radiation Effects in Solids*, 2007, pp. 1–23.
- 46 T. Nishizaka, R. Seo, H. Tadakuma, K. Kinoshita Jr and S. Ishiwata, *Biophys. J.*, 2000, **79**, 962–974.
- 47 H. Lee, B. Pelz, J. Ferrer, T. Kim, M. Lang and R. Kamm, *Cell. Mol. Bioeng.*, 2009, **2**, 28–38.
- 48 D. Boal, *Mechanics of the Cell*, Cambridge University Press, 2002.
- 49 G. Hummer and A. Szabo, *Biophys. J.*, 2003, **85**, 5–15.
- 50 J. Åström, P. Kumar, I. Vattulainen and M. Karttunen, *Phys. Rev. E: Stat., Nonlinear, Soft Matter Phys.*, 2008, **77**, 051913.
- 51 A. Argon, *Strengthening Mechanisms in Crystal Plasticity*, Oxford University Press, USA, 2008, vol. 4.
- 52 K. Kasza, C. Broedersz, G. Koenderink, Y. Lin, W. Messner, E. Millman, F. Nakamura, T. Stossel, F. MacKintosh and D. Weitz, *Biophys. J.*, 2010, **99**, 1091–1100.
- 53 O. Lieleg and A. Bausch, *Phys. Rev. Lett.*, 2007, **99**, 158105.
- 54 R. Tharmann, M. Claessens and A. Bausch, *Phys. Rev. Lett.*, 2007, **98**, 88103.
- 55 C. Broedersz, K. Kasza, L. Jawerth, S. Münster, D. Weitz and F. MacKintosh, *Soft Matter*, 2010, **6**, 4120–4127.
- 56 E. Peña, *J. Mech. Phys. Solids*, 2011, **59**, 1808–1822.
- 57 J. Planas, G. Guinea and M. Elices, *Phys. Rev. E: Stat., Nonlinear, Soft Matter Phys.*, 2007, **76**, 041903.
- 58 A. Zaccone and E. Scossa-Romano, *Phys. Rev. B: Condens. Matter Mater. Phys.*, 2011, **83**, 184205.
- 59 C. Storm, J. Pastore, F. MacKintosh, T. Lubensky and P. Janmey, *Nature*, 2005, **435**, 191–194.
- 60 S. Furuike, T. Ito and M. Yamazaki, *FEBS Lett.*, 2001, **498**, 72–75.
- 61 D. Head, A. J. Levine and F. C. MacKintosh, *Phys. Rev. Lett.*, 2003, **91**, 108102.
- 62 C. Heussinger, B. Schaefer and E. Frey, *Phys. Rev. E: Stat., Nonlinear, Soft Matter Phys.*, 2007, **76**, 031906.
- 63 C. Broedersz, X. Mao, T. Lubensky and F. MacKintosh, *Nat. Phys.*, 2011, **7**, 983–988.
- 64 S. Winder and K. Ayscough, *J. Cell Sci.*, 2005, **118**, 651–654.
- 65 G. Žagar, P. Onck and E. Giessen, *IUTAM symposium on cellular, molecular and tissue mechanics*, 2010, pp. 161–169.
- 66 M. Bai, A. Missel, A. Levine and W. Klug, *Acta Biomater.*, 2010, **7**, 2109–2118.
- 67 J. Howard, *Mechanics of motor proteins and the cytoskeleton*, Sinauer Associates Sunderland, MA, 2001.

Addition and correction

[View Online](#)

Note from RSC Publishing

This article was originally published with incorrect page numbers. This is the corrected, final version.

The Royal Society of Chemistry apologises for these errors and any consequent inconvenience to authors and readers.
